Electronic Supplementary Material (ESI) for Environmental Science: Processes & Impacts.

Electronic Supplementary Information for

Photodecay of guaiacol is faster in ice, and even more rapid on ice, than in aqueous solution

Ted Hullar, Fernanda Bononi, Zekun Chen, Danielle Magadia, Oliver Palmer,
Theo Tran, Dario Rocca, Oliviero Andreussi, Davide Donadio, and Cort Anastasio

resubmitted to Environmental Science: Processes and Impacts
27 June 2020

Supplementary Section S1. Determining absolute photon fluxes from available measurements

Here, we determine absolute photon fluxes in our experimental system using the measured value for 2-nitrobenzaldehyde (2NB) photolysis on a given day and the relative photon fluxes we measured for a given light condition.

Begin with the equation for j_{2NB}, our experimentally determined photodecay rate constant for 2NB:

$$j_{2NB,exp} = \frac{2303}{N_A} \Phi_{2NB,\lambda} \sum_{\lambda} (\varepsilon_{2NB,\lambda} \ I_{\lambda} \ \Delta\lambda) \qquad \text{(S1)}$$

where 2303 is a factor for unit and base (base-10 to base-e) conversions (1000 cm^3 L^{-1}), N_A is Avogadro's number (6.022 x 10^{23} mlc mol^{-1}), $\Phi_{2NB,\lambda}$ is the quantum yield for loss of 2NB (molecule $photon^{-1}$), $\varepsilon_{2NB,\lambda}$ is the wavelength-dependent molar absorptivity for 2NB (M^{-1} cm^{-1}), I_{λ} is the photon flux at each wavelength (photons cm^{-2} s^{-1} nm^{-1}), and Δλ is the wavelength interval between photon flux data points (1 nm for this work). $\Phi_{2NB,\lambda}$ and $\varepsilon_{2NB,\lambda}$ are from [17]; the quantum yield is independent of wavelength above 280 nm. We measured $j_{2NB,exp}$ on each experiment day, as described in section 2.3, and I^{meas}_{λ} (relative photon flux counts) using a TIDAS spectrophotometer (World Precision Instruments) for both LC1 and LC2 conditions. At a specific illumination position, measured counts and actual photon fluxes are related by:

$$I_{\lambda} = I_{\lambda}^{meas} \ SF \qquad \text{(S2)}$$

where I^{meas}_{λ} is the measured relative photon count at each wavelength (counts) and *SF* is a scaling factor (photons cm^{-2} s^{-1} nm^{-1} $count^{-1}$). Substituting S2 into S1 and rearranging gives

$$SF = \frac{j_{2NB,exp}}{\frac{2303}{N_A} \Phi_{2NB,\lambda} \sum_{\lambda} (\varepsilon_{2NB,\lambda} \, I_{\lambda}^{meas} \ \Delta\lambda)} \qquad \text{(S3)}$$

substituting S2 into S3 gives

$$I_{\lambda} \ = I_{\lambda}^{meas} \frac{j_{2NB,exp}}{\frac{2303}{N_A} \Phi_{2NB,\lambda} \sum_{\lambda} (\varepsilon_{2NB,\lambda} \, I_{\lambda}^{meas} \ \Delta\lambda)} \qquad \text{(S4)}$$

Applying S1 to guaiacol gives:

$$j_{GUA,exp} = \frac{2303}{N_A} \Phi_{GUA} \sum_{\lambda} (\varepsilon_{GUA,\lambda} \; I_{\lambda} \, \Delta\lambda) \qquad \text{(S5)}$$

where Φ_{GUA} is the average quantum yield for loss of guaiacol and $\varepsilon_{GUA,\lambda}$ is the wavelength-dependent molar absorptivity for guaiacol. We have measured $\varepsilon_{GUA,\lambda}$ (Figure 3), and I_λ was determined in S4. Finally, we solve S5 for $\Phi_{GUA,\lambda}$ to determine the average quantum yield for guaiacol photodecay across the absorption range.

The rate constant for light absorption by guaiacol, $j_{h\nu\ abs}$ (photons molecule^{-1} s^{-1}), is simply the rate constant for loss divided by the quantum yield for loss, i.e.,

$$j_{h\nu\ abs} = \frac{2303}{N_A} \sum_{\lambda} (\varepsilon_{GUA,\lambda} \; I_{\lambda} \, \Delta\lambda) \qquad \text{(S6)}$$

Combining S5 and S6 gives a simplified form of S5:

$$j_{GUA,exp} = \Phi_{GUA} \; j_{h\nu\ abs} \qquad \text{(S7)}$$

Supplementary Section S2. Computational Methods – additional details

First-principles MD (FPDM) simulations of guaiacol are carried out in aqueous solution and at the air-ice interface using the CP2K-Quickstep package. [1, 2] Aqueous solution simulations were carried out at 300K in a cubic simulation box (12:8 Å) containing 64 water molecules while simulations of molecule adsorbed on the ice surface were carried out at 263K with one molecule on the surface of an ice slab made of 192 water molecules in a orthorhombic cell (18×15.589×80 Å3) with periodic boundary conditions (PBC). The models utilized for these runs were built based on previous data obtained from classical MD simulations using the LAMMPS free software package. [3] Simulations are carried out at the NVT ensemble, in which temperature is controlled by stochastic velocity rescaling. [4] The Perdew-Burke-Ernzerhof (PBE) generalized gradient approximation (GGA) was used for the exchange and correlation functional [5], while valence Kohn-Sham orbitals are represented on a double-ζ localized basis set[6], and core states are treated implicitly using Geodecker-Teter-Hutter pseudopotentials. [7] Hydrogen atoms are replaced with deuterium, thus allowing a relatively large timestep of 0.5 fs to integrate the equations of motion.

We performed production runs of 50 ps and extracted up to 200 statistically independent frames from each trajectory in order to compute the UV-visible absorption spectra using the ensemble approach. [8, 9] Aqueous solutions are equilibrated at room temperature (300 K), whereas ice slabs are kept at 263 K.

Absorption spectra calculations were performed with the turboTDDFT software package, [10, 11] using the recursive Lanczos algorithm [12] with the plane-wave potential method. [13] Spectra calculations are performed on hundreds of frames obtained from FPMD simulation runs for both aqueous solution and the air-ice interface in tetragonal simulation cells of dimensions 25×25×50 Å3, with long-range electrostatic corrections.[14] Explicit water molecules are removed and substituted by a self-consistent continuum solvation (SCCS) model in order to reduce computational costs. This model is implemented the ENVIRON add-on [15] on Quantum Espresso. The homogeneous medium for calculations in solution is characterized by the dielectric constant of water at 300K, and for calculations on the ice surface, we set up solvent exclusion regions, where each region is represented by their dielectric constants. The transition between the two different regions is smoothed by a smearing function.

To build the least absolute shrinkage and selection operator (LASSO) regression model, [16] 184 frames from a FPMD trajectory of guaiacol in solution and 141 frames in air-ice interface, along with their lowest transition energy from the TDDFT calculations, were used as the input data. A regularization rate a of 10-8 was utilized and the 5-fold cross validation scheme was performed along with the training and testing process. The developed model was applied to initially predict the absorbance for 4882 frames obtained from a trajectory of guaiacol in solution. Afterwards, the same model was applied to 4861 frames of guaiacol on the ice surface. Both spectra were then generated with the Gaussian envelope with a width of 0.0136 eV.

Supplementary Section S3. Snow machine principles, design, and snow production

The general design of the snow-making machine is based on work from [19] and [20]. Supplementary Figure S2a shows a flow diagram diagram of machine operation. First, cold air is blown into the machine by two fans (combined airflow rate 4 m^3 min^{-1}) and passes over a pan of warm water (45 °C), where the air becomes supersaturated with water vapor. This moist air then enters a second chamber that contains a rack crossed by horizontal nylon lines. Water from the supersaturated air initially nucleates on the lines; additional water condenses on the growing snow crystals. The remaining air exits the chamber, where excess moisture is trapped by a mesh fabric (mesh size approximately 0.5 mm; not shown). The machine is approximately 1 m x 2 m x 1 m tall.

Supplementary Figure S2b presents an oblique view of the machine in the cold room (average temperature -15 °C) showing detail of several parts, including the intake fans and the snow collection bin. The section containing the water pan is insulated by 5 cm expanded polystyrene insulation (top and front insulation has been removed for clarity). Pan water temperature is held to ± 1 °C by a thermostatically controlled resistive heating element. To run the machine, we place 3 L MQ water in the pan, then start the fans and heater (the chamber door shown open here is closed during operation). After ~4 hours, we collect the snow by shaking the rack containing the nylon lines, causing the snow to drop into the collection bin. We gently shake the snow in the bin to mix it and simulate natural weathering, the proceed with further treatment as described in the text.

The machine typically produces ~50-75 g of dendritic snow per hour, typical snow is shown in Supplementary Figure S3. Figure S3a depicts crystals hanging from the nylon lines in the chamber; crystals grown downward. Overall crystal length, which often includes side branches, is 10-15 mm after 4 hours of growth (Supplementary Figures S3b and S3c). After the snow falls into the bin and is mixed (Figure S3d), density is approximately 5%.

Date	Initial conc (uM)	Beaker size (ml)	Ill. Time (min)	j_{GUA} (min^{-1})	j_{GUA} SE	$k'_{GUA,dark}$ (min^{-1})	$k'_{GUA,dark}$ SE	$j_{GUA,exp}$ (min^{-1})	$j_{GUA,exp}$ SE	j_{2NB} (s^{-1})	j_{2NB} SE	j^*_{GUA} (min^{-1}/s^{-1})	j^*_{GUA} SE
Aqueous, LC1													
20170306	10	5	180	0.00085	0.00006	0.00041	0.00003	0.00044	0.00007	0.0053	0.0001	0.084	0.01
20170309	1.0	5	300	0.00067	0.00004	0.00024	0.00002	0.00043	0.00005	0.0053	0.0001	0.080	0.01
20170411	1.0	10	250	0.00094	0.00010	0.00043	0.00021	0.00051	0.00023	0.0061	0.0002	0.084	0.04
20170411	1.0	10	250	0.00036	0.00004	-0.00004	0.00004	0.00036	0.00006	0.0061	0.0002	0.059	0.01
20170413	1.0	10	265	0.00067	0.00007	0.00040	0.00005	0.00027	0.00009	0.0045	0.0001	0.060	0.02
20170413	1.0	10	265	0.00037	0.00003	-0.00003	0.00006	0.00037	0.00006	0.0045	0.0001	0.083	0.01
Aqueous, LC2													
20191230	1.0	10	1834	0.00005	0.00004	0.00003	0.00002	0.00002	0.00005	0.0035	0.0001	0.006	0.01
20200110	1.0	10	1674	0.00009	0.00001	0.00005	0.00001	0.00004	0.00002	0.0034	0.0001	0.013	0.01
20200306	1.0	10	1748	0.00003	0.00000	0.00000	0.00000	0.00003	0.00001	0.0038	0.0001	0.008	0.00
Freezer frozen solution, LC1													
20170419	1.0	10	239	0.00138	0.00046	0.00067	0.00003	0.00071	0.00046	0.0065	0.0001	0.109	0.07
20170424	1.0	10	160	0.00152	0.00020	0.00016	0.00004	0.00136	0.00021	0.0041	0.0006	0.330	0.07
20170425	1.0	10	235	0.00092	0.00020	0.00012	0.00009	0.00080	0.00022	0.0044	0.0002	0.183	0.05
20170425	1.0	10	225	0.00068	0.00021	-0.00028	0.00038	0.00068	0.00043	0.0044	0.0002	0.155	0.10
20170426	1.0	10	200	0.00063	0.00026	-0.00019	0.00041	0.00063	0.00048	0.0045	0.0003	0.139	0.11
20170426	1.0	10	200	0.00115	0.00029	-0.00003	0.00025	0.00115	0.00039	0.0045	0.0003	0.255	0.09
Freezer frozen solution, LC2													
20200101	1.0	10	1757	0.00013	0.00004	0.00001	0.00002	0.00013	0.00004	0.0026	0.0003	0.049	0.02
20200114	1.0	10	1575	0.00025	0.00005	0.00008	0.00003	0.00017	0.00005	0.0029	0.0005	0.057	0.02
20200310	1.0	10	1629	0.00022	0.00006	0.00004	0.00002	0.00018	0.00007	0.0029	0.0009	0.062	0.03
Liquid nitrogen frozen solution, LC1													
20170501	1.0	10	200	0.00123	0.00015	0.00026	0.00023	0.00097	0.00028	0.0047	0.0000	0.207	0.06
20170501	1.0	10	200	0.00115	0.00029	-0.00003	0.00025	0.00115	0.00039	0.0047	0.0000	0.245	0.08
20170503	1.0	10	150	0.00174	0.00015	0.00044	0.00017	0.00130	0.00023	0.0043	0.0002	0.305	0.06
20170503	1.0	10	150	0.00103	0.00014	-0.00017	0.00006	0.00103	0.00015	0.0043	0.0002	0.243	0.04
Liquid nitrogen frozen solution, LC2													
20200203	1.0	10	1919	0.00011	0.00002	0.00000	0.00001	0.00011	0.00002	0.0025	0.0002	0.044	0.01
20200221	1.0	10	1513	0.00018	0.00002	0.00004	0.00003	0.00014	0.00004	0.0025	0.0002	0.056	0.01
20200303	1.0	10	1677	0.00018	0.00005	-0.00007	0.00004	0.00018	0.00006	0.0042	0.0003	0.042	0.01
Vapor-deposited to ice, LC1													
20170510	0.029	10	200	0.01103	0.00133	0.00525	0.00232	0.00578	0.00268	0.0050	0.0005	1.159	0.55
20170517	3.5	10	225	0.00064	0.00044	0.00035	0.00034	0.00029	0.00056	0.0041	0.0009	0.071	0.14
20170522	9.0	10	300	0.00462	0.00074	0.00108	0.00103	0.00354	0.00127	0.0032	0.0008	1.110	0.48
20170522	6.0	10	300	0.00235	0.00096	0.00077	0.00170	0.00158	0.00195	0.0032	0.0008	0.495	0.62
Vapor-deposited to snow, LC1													
20170313	0.3	5	150	0.00298	0.00026	0.00053	0.00044	0.00245	0.00051	0.0019	0.00005	1.288	0.27
20170314	1.2	5	150	0.00738	0.00070	0.00345	0.00019	0.00393	0.00072	0.0019	0.00005	2.066	0.38
20170316	2.2	5	150	0.00559	0.00032	0.00389	0.00064	0.00170	0.00071	0.0020	0.00015	0.867	0.37
20170327	9.0	10	100	0.00366	0.00068	0.00223	0.00111	0.00143	0.00130	0.0024	0.00008	0.589	0.53
20170403	3.0	10	150	0.00328	0.00032	0.00076	0.00033	0.00252	0.00046	0.0024	0.00008	1.037	0.19
20170404	0.6	10	125	0.00665	0.00183	0.00235	0.00115	0.00430	0.00216	0.0024	0.00009	1.815	0.92
Vapor-deposited to snow, LC2													
20191219	2.0	10	1525	0.00082	0.00023	0.00051	0.00012	0.00031	0.00026	0.0010	0.0001	0.297	0.25
20200122	0.3	10	1366	0.00131	0.00030	0.00035	0.00021	0.00096	0.00037	0.0011	0.0000	0.874	0.34
20200317	2.5	10	1547	0.00086	0.00012	0.00009	0.00006	0.00077	0.00014	0.0010	0.0001	0.769	0.15
20200319	2.8	10	256	0.00082	0.00040	-0.00033	0.00029	0.00082	0.00050	0.0011	0.0000	0.774	0.47

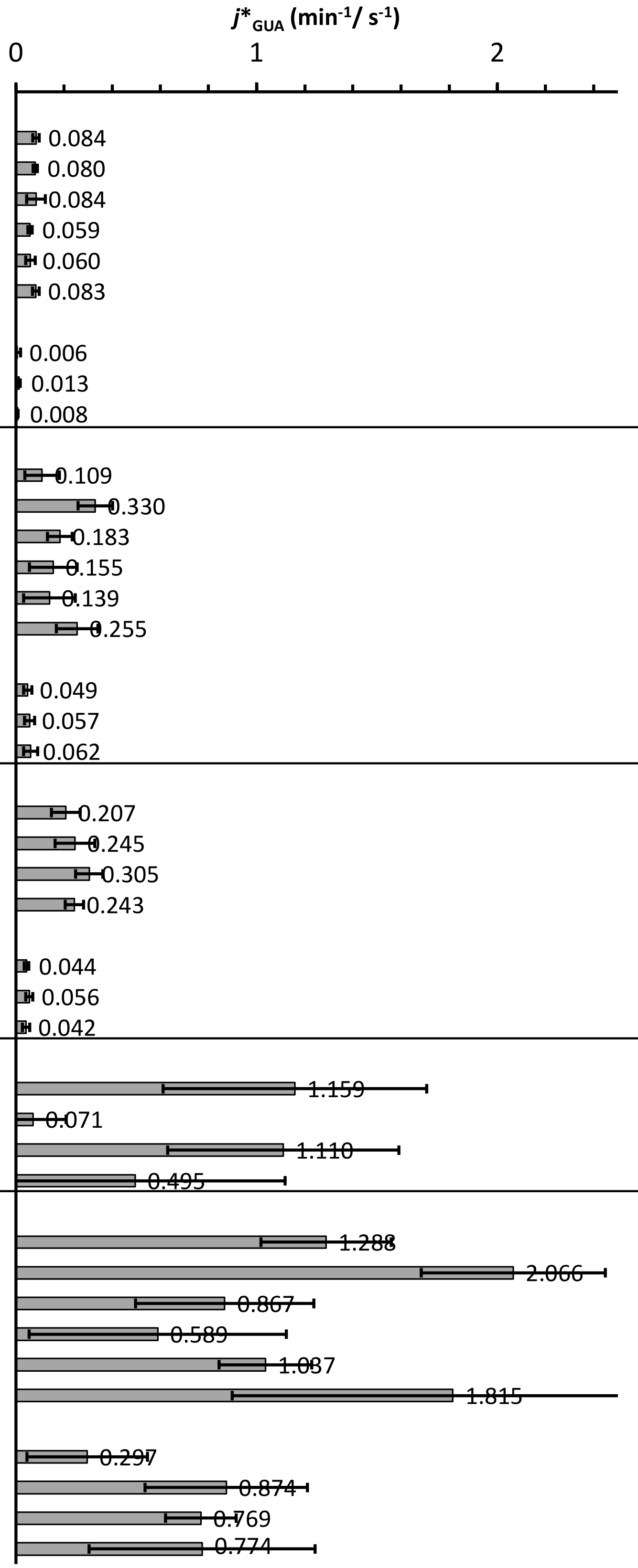

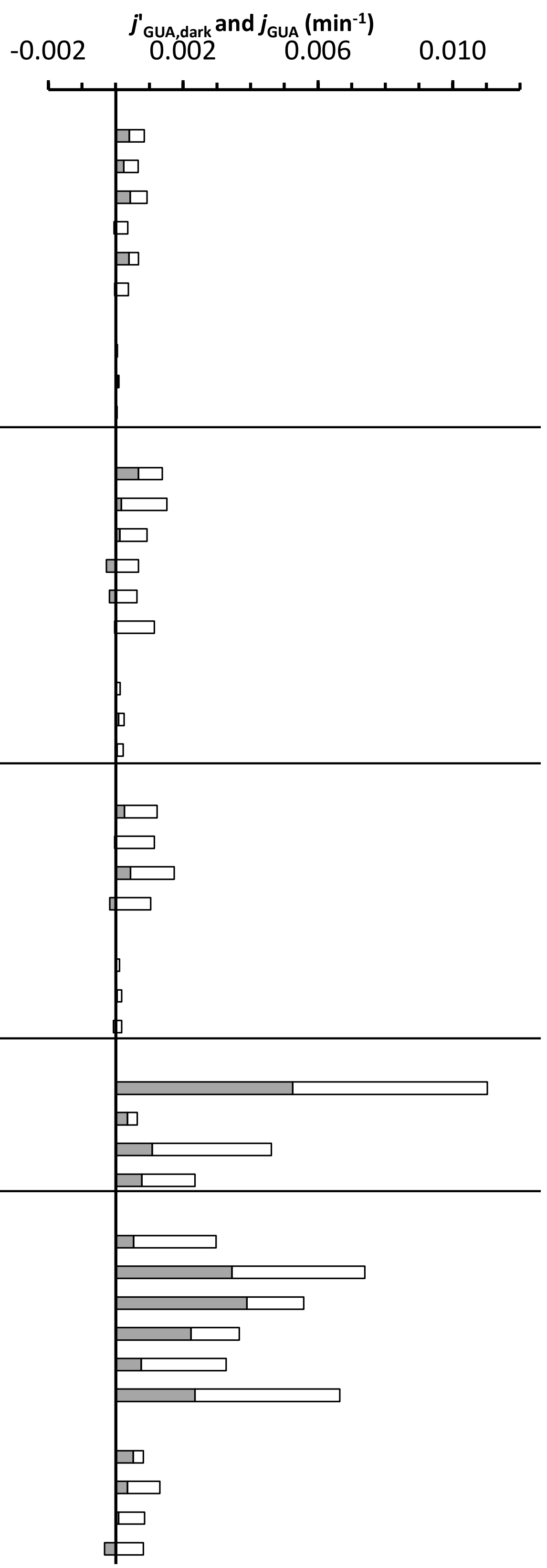

Supplemental Table S1. Experimental results for individual experiments. See text for additional details. LC1 (Light Condition 1) samples were illuminated with the output of a 1000 W arc lamp filtered through an air mass filter. LC2 (Light Condition 2) samples were illuminated with light which passed through the air mass filter, a 295 long pass filter, and 400 short pass filter. LC2 snow samples were also tamped by pushing the snow surface 10 mm below the lip of the sample beaker; LC1 snow samples were not tamped.

	Num.	j_{GUA} (min^{-1})			$k'_{GUA,dark}$ (min^{-1})			$j_{GUA,exp}$ (min^{-1})			j^*_{GUA} (min^{-1}/s^{-1})			j_{2NB} (s^{-1})		
	samp.	avg	SD	95% CI	avg	SD	95% CI	avg	SD	95% CI	avg	SD	95% CI	avg	SD	95% CI
LC1																
Aqueous	6	6.4E-04	2.4E-04	2.5E-04	2.3E-04	2.2E-04	2.3E-04	4.0E-04	8.1E-05	8.5E-05	7.5E-02	1.2E-02	1.3E-02	5.3E-03	7.0E-04	7.3E-04
Freezer frozen solution	6	1.0E-03	3.7E-04	3.9E-04	7.8E-05	3.4E-04	3.5E-04	8.9E-04	3.0E-04	3.1E-04	2.0E-01	8.2E-02	8.6E-02	4.7E-03	8.6E-04	9.1E-04
Liquid nitrogen frozen solution	4	1.3E-03	3.1E-04	4.9E-04	1.2E-04	2.8E-04	4.4E-04	1.1E-03	1.4E-04	2.3E-04	2.5E-01	4.0E-02	6.4E-02	4.5E-03	2.5E-04	3.9E-04
Vapor-deposited to ice surface	4	4.7E-03	4.6E-03	7.2E-03	1.9E-03	2.3E-03	3.6E-03	2.8E-03	2.4E-03	3.8E-03	7.1E-01	5.2E-01	8.3E-01	3.9E-03	8.6E-04	1.4E-03
Vapor-deposited to snow	6	4.9E-03	1.9E-03	2.0E-03	2.2E-03	1.4E-03	1.4E-03	2.7E-03	1.2E-03	1.2E-03	1.3E+00	5.7E-01	6.0E-01	2.2E-03	2.7E-04	2.8E-04
LC2																
Aqueous	3	5.9E-05	3.2E-05	7.9E-05	2.8E-05	2.3E-05	5.7E-05	3.1E-05	1.3E-05	3.1E-05	8.8E-03	3.8E-03	9.6E-03	3.6E-03	2.4E-04	5.9E-04
Freezer frozen solution	3	2.0E-04	6.0E-05	1.5E-04	4.3E-05	3.7E-05	9.3E-05	1.6E-04	2.7E-05	6.7E-05	5.6E-02	6.3E-03	1.6E-02	2.8E-03	1.9E-04	4.8E-04
Liquid nitrogen frozen solution	3	1.6E-04	3.8E-05	9.4E-05	-1.3E-05	5.3E-05	1.3E-04	1.4E-04	3.3E-05	8.1E-05	4.8E-02	7.5E-03	1.9E-02	3.1E-03	9.6E-04	2.4E-03
Vapor-deposited to ice surface	0															
Vapor-deposited to snow	4	9.5E-04	2.4E-04	3.8E-04	1.6E-04	3.7E-04	5.9E-04	7.1E-04	2.8E-04	4.5E-04	6.8E-01	2.6E-01	4.1E-01	1.0E-03	4.1E-05	6.5E-05

Supplementary Table S2. Statistical summary parameters for the various sample treatments. 95% CI is the 95% confidence interval of the mean for each sample treatment.

Date	Bubbling time (min)	Ill. Time (min)	j_{GUA} (min^{-1})	j_{GUA} SE	$k'_{GUA,dark}$ (min^{-1})	$k'_{GUA,dark}$ SE	$j_{GUA,exp}$ (min^{-1})	$j_{GUA,exp}$ SE	j_{2NB} (s^{-1})	j_{2NB} SE	j^*_{GUA} (min^{-1}/s^{-1})	j^*_{GUA} SE
Aqueous, LC1												
20170606	0	270	0.00067	0.00009	0.00031	0.00007	0.00036	0.00011	0.0076	0.0000	0.048	0.01
20170606	2	270	0.00023	0.00003	0.00005	0.00009	0.00018	0.00009	0.0076	0.0000	0.024	0.01
20170612	2	279	0.00036	0.00003	0.00000	0.00004	0.00036	0.00005	0.0077	0.0001	0.047	0.01
20170612	0	270	0.00022	0.00004	0.00002	0.00003	0.00020	0.00005	0.0077	0.0001	0.026	0.01
20170720	4	270	0.00013	0.00009	-0.00001	0.00003	0.00013	0.00009	0.0071	0.0001	0.018	0.01
20170720	0	270	0.00027	0.00006	0.00011	0.00014	0.00016	0.00016	0.0071	0.0001	0.022	0.02
20170724	0	300	0.00040	0.00005	0.00019	0.00005	0.00021	0.00007	0.0070	0.0001	0.030	0.01
20170724	4	300	0.00019	0.00002	0.00003	0.00003	0.00016	0.00004	0.0070	0.0001	0.023	0.01
Frozen solution, LC1												
20170609	0	270	0.00133	0.00009	0.00047	0.00006	0.00086	0.00011	0.0073	0.0000	0.118	0.01
20170609	2	270	0.00059	0.00008	0.00005	0.00003	0.00054	0.00009	0.0073	0.0000	0.074	0.01
20170613	0	270	0.00128	0.00011	0.00032	0.00007	0.00096	0.00013	0.0075	0.0001	0.128	0.02
20170613	4	270	0.00056	0.00006	-0.00021	0.00006	0.00056	0.00009	0.0075	0.0001	0.075	0.01
20170718	4	270	0.00066	0.00009	0.00005	0.00010	0.00061	0.00013	0.0072	0.0001	0.085	0.02
20170718	0	270	0.00093	0.00012	-0.00007	0.00018	0.00093	0.00021	0.0072	0.0001	0.129	0.03

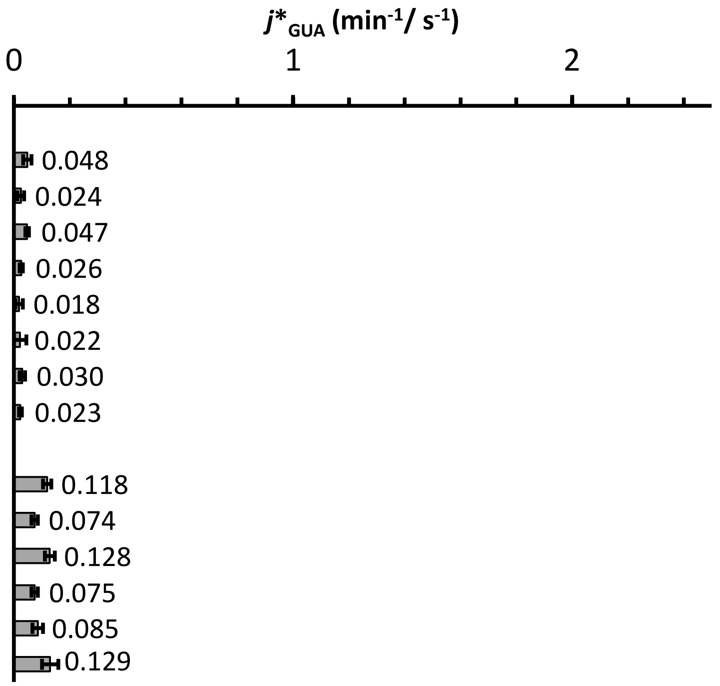

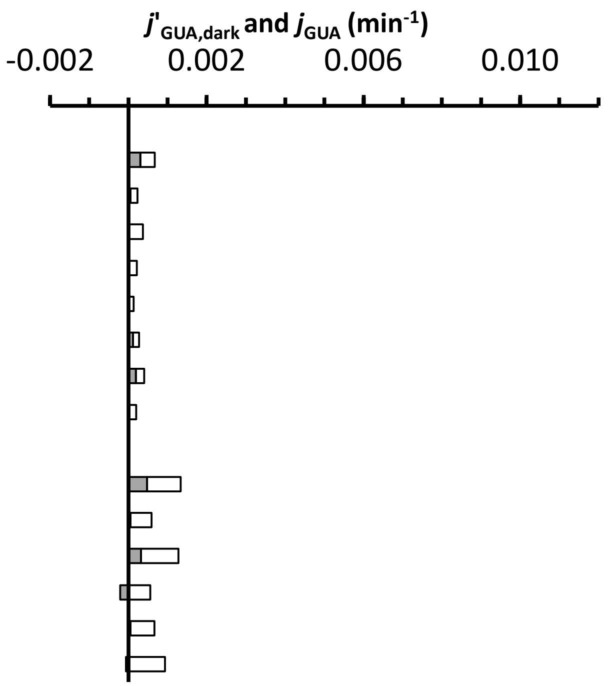

Supplemental Table S3. Similar data as Supplemental Table 1, but for experiments bubbled with nitrogen. See text for additional details. All samples had an initial GUA concentration of 1 µM. Samples were bubbled and illuminated in the same container (2 ml HPLC vials with PTFE-lined caps). Because these experiments were conducted in different containers, these data were only used to assess the impact of dissolved oxygen and are not included in Supplemental Table 1 or any other experimental results.

Wavelength (nm)	Molar absorptivity (M^{-1} cm^{-1})	Wavelength (nm)	Molar absorptivity (M^{-1} cm^{-1})	Wavelength (nm)	Molar absorptivity (M^{-1} cm^{-1})
317	0.000463	287	412	257	633
316	0.000734	286	606	256	563
315	0.00116	285	861	255	497
314	0.00184	284	1168	254	436
313	0.00292	283	1464	253	389
312	0.00463	282	1721	252	345
311	0.00735	281	1880	251	311
310	0.0116	280	1979	250	280
309	0.0185	279	2057		
308	0.0293	278	2144		
307	0.0464	277	2252		
306	0.0735	276	2327		
305	0.116	275	2360		
304	0.185	274	2351		
303	0.293	273	2321		
302	0.464	272	2251		
301	0.735	271	2175		
300	1.17	270	2082		
299	1.85	269	1983		
298	2.93	268	1877		
297	4.64	267	1763		
296	7.36	266	1646		
295	12.4	265	1523		
294	19.1	264	1388		
293	31.4	263	1260		
292	48.7	262	1131		
291	77.3	261	1019		
290	120	260	915		
289	182	259	813		
288	280	258	721		

Supplementary Table S4. Guaiacol molar absorptivities ($\varepsilon_{GUA,\lambda}$). For wavelengths 250-296 nm, we measured absorbance spectra in five aqueous guaiacol solutions (10-1000 µM) at 25 °C using a UV-2501PC spectrophotometer (Shimadzu) in 1.0 cm cuvettes against a MQ reference cell. For each wavelength, we calculated the base-10 molar absorptivity as the slope of the linear regression of measured absorbance versus the guaiacol concentration. To determine values from 297-317 nm, where experimental data was variable, we used the measured data from 290-296 nm, plotted λ vs $\ln(\varepsilon_{GUA,\lambda})$, then used the slope of the linear regression to determine $\varepsilon_{GUA,\lambda}$.

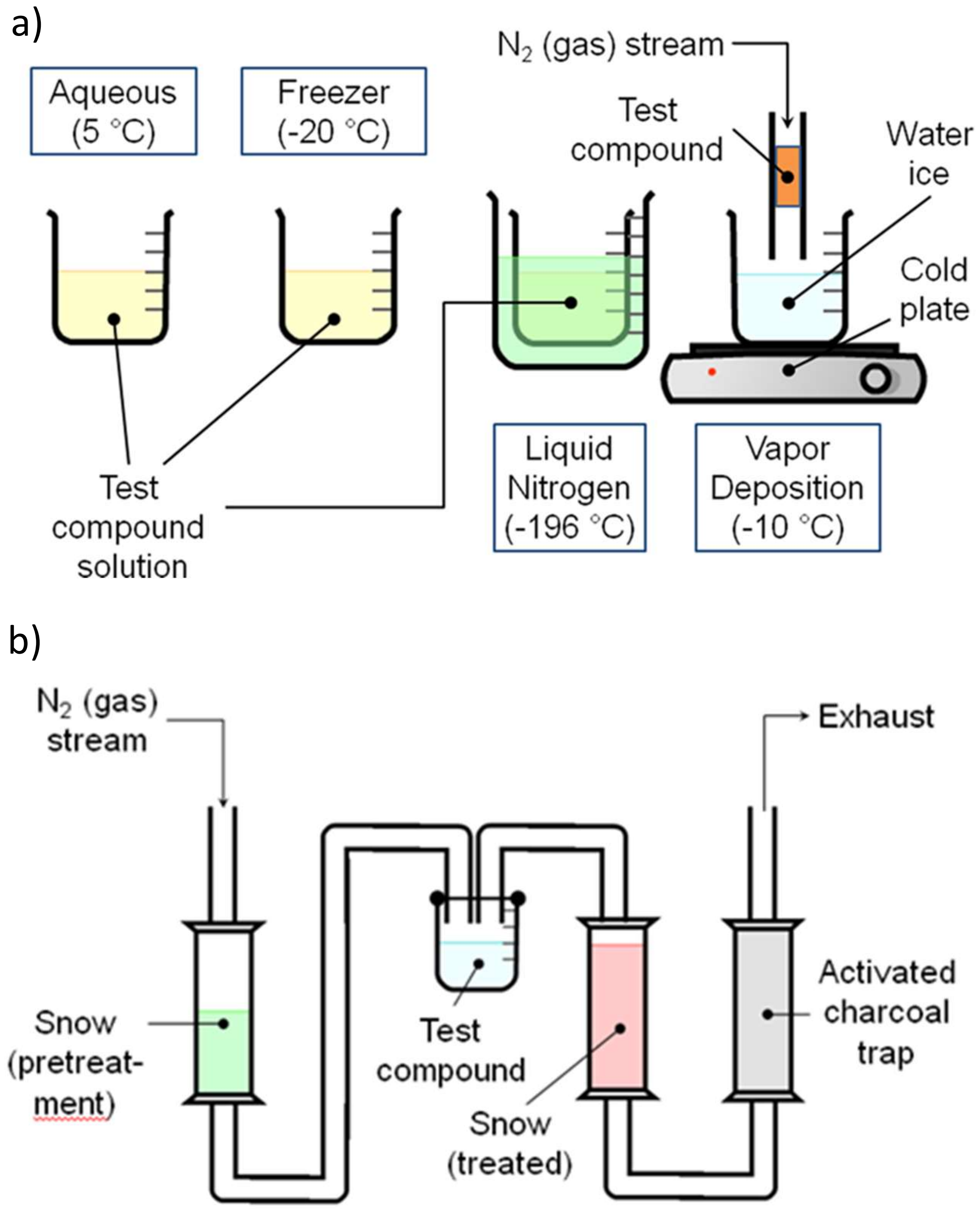

Supplementary Figure S1. Sample preparation methods. See text for additional details. a) Diagram of sample preparation methods (except for vapor-deposited to snow, which is shown in panel b), taken from [18]. b) Apparatus to vapor-deposit guaiacol to nature-identical snow.

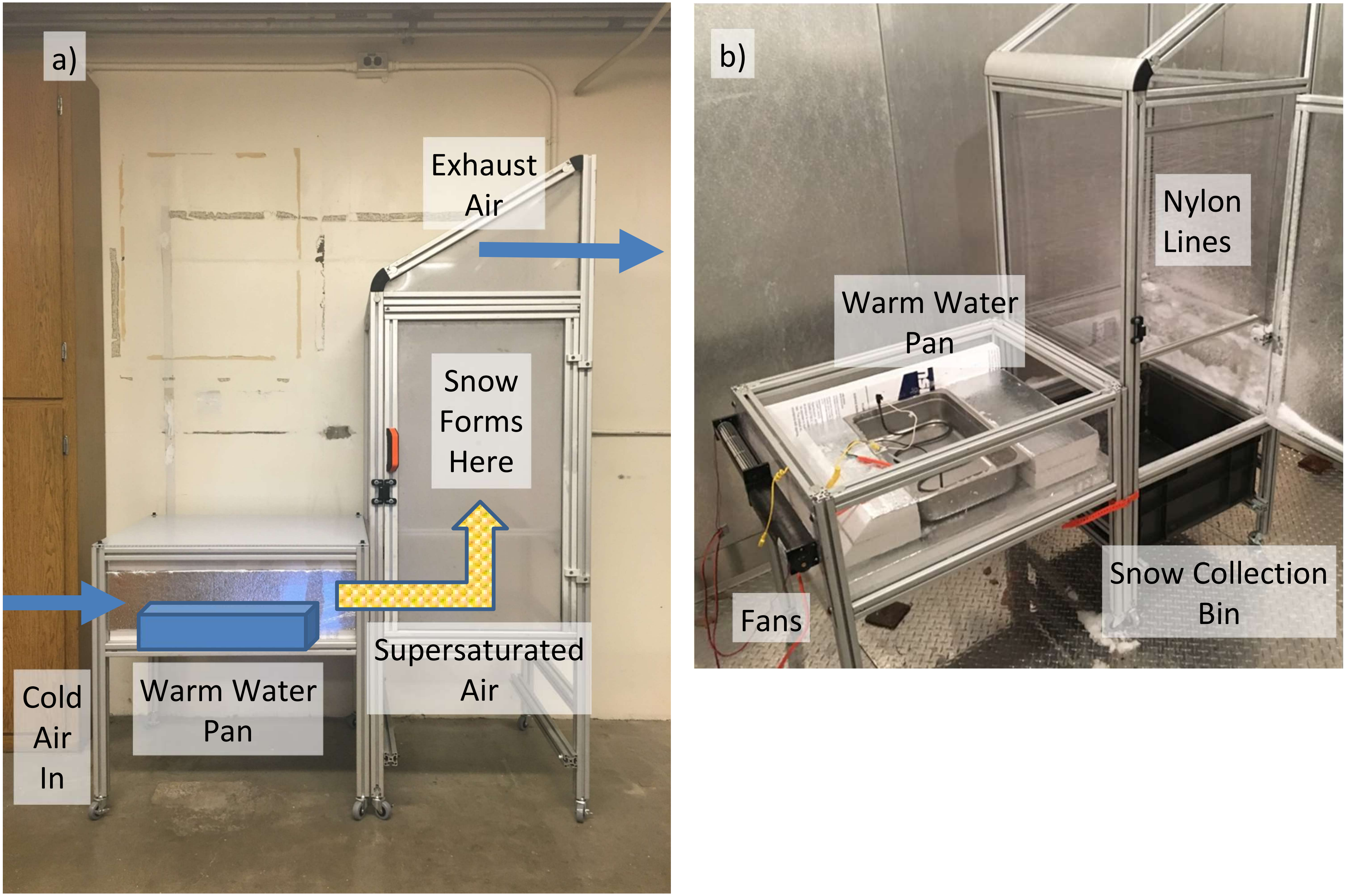

Supplementary Figure S2. Photographs of snow-making machine. a) Diagram showing principles of operation, including airflow. b) Snow machine in cold room, showing mechanical details, including water pan and snow collection bin. See Supplementary Section S2 for additional information.

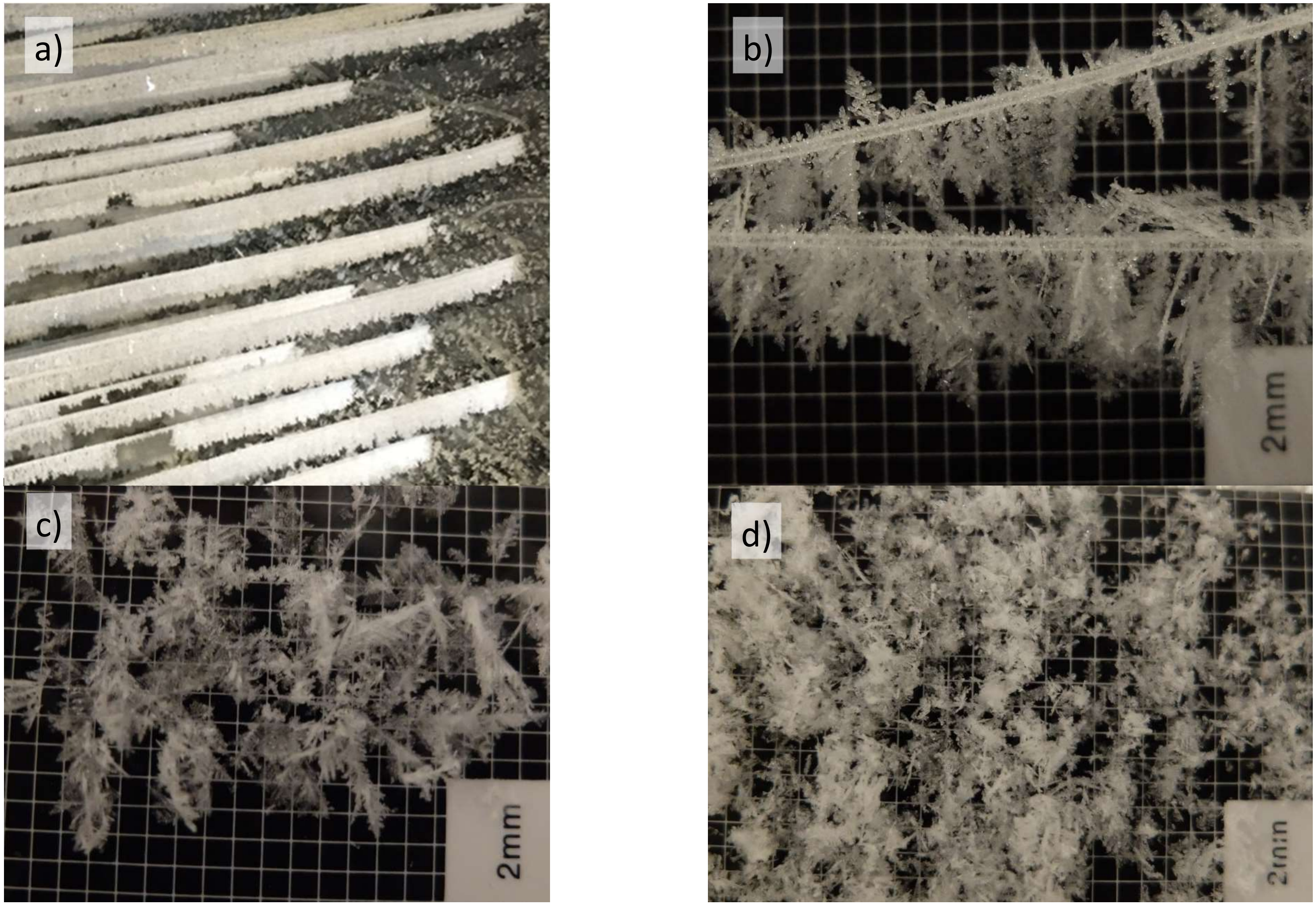

Supplementary Figure S3. Images of nature-identical snow. a) Snow crystals growing on nylon lines in the snow machine; airflow is from bottom to top in this image. b) detail image of panel a), showing dendritic snow growth on nylon lines. c) Snow crystals after being knocked off the nylon wires. d) Snow crystals after being gently mixed in the snow tub (to simulate natural weathering) but before treatment with guaiacol. Snow density at this stage is around 5%; after treatment and transfer to the beakers for illumination, the final density was approximately 10%.

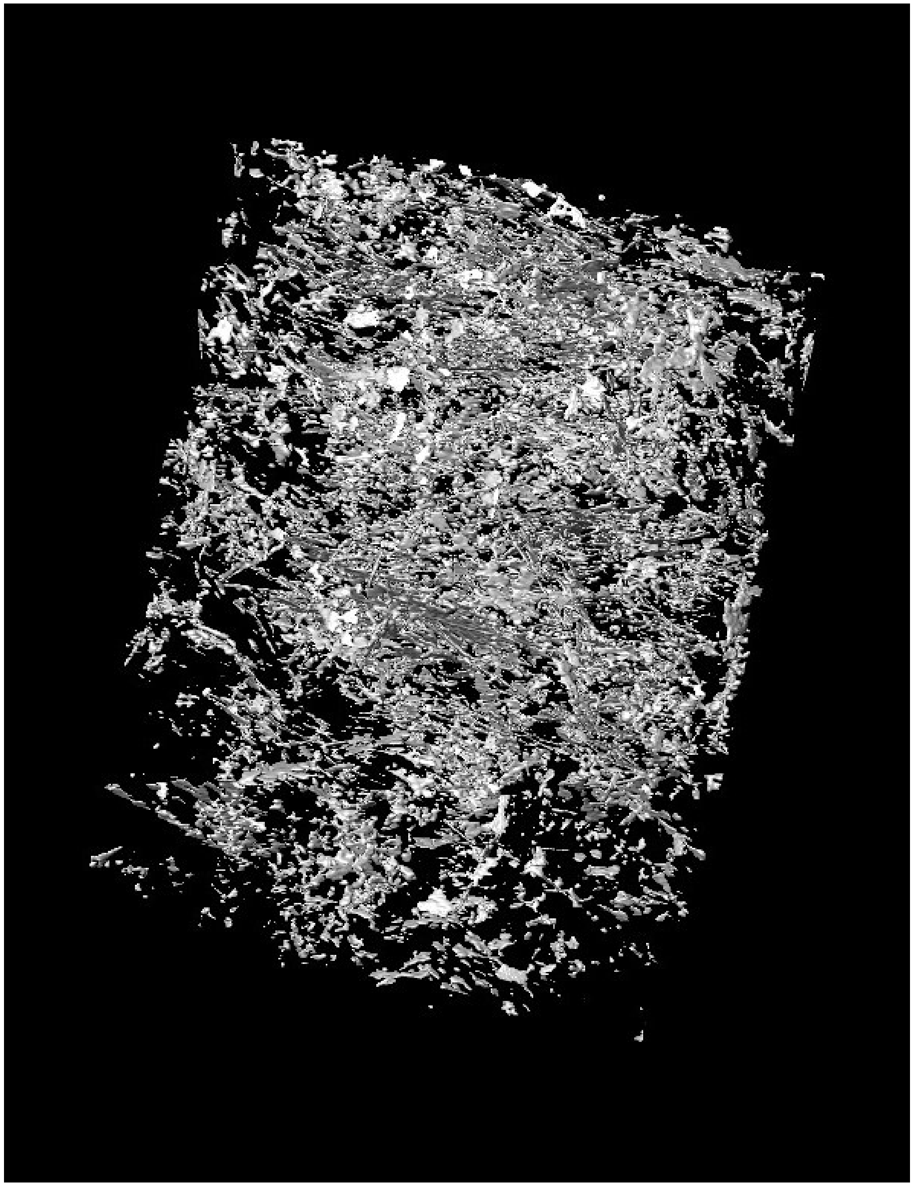

Supplementary Figure S4. Micro-computed tomography (microCT) image of snow after placement into beaker for illumination. Beaker inside diameter is approximately 1 cm; snow-filled portion is approximately 1.5 cm high. For a more realistic visualization of the snow, please see Supplemental Movie M1.

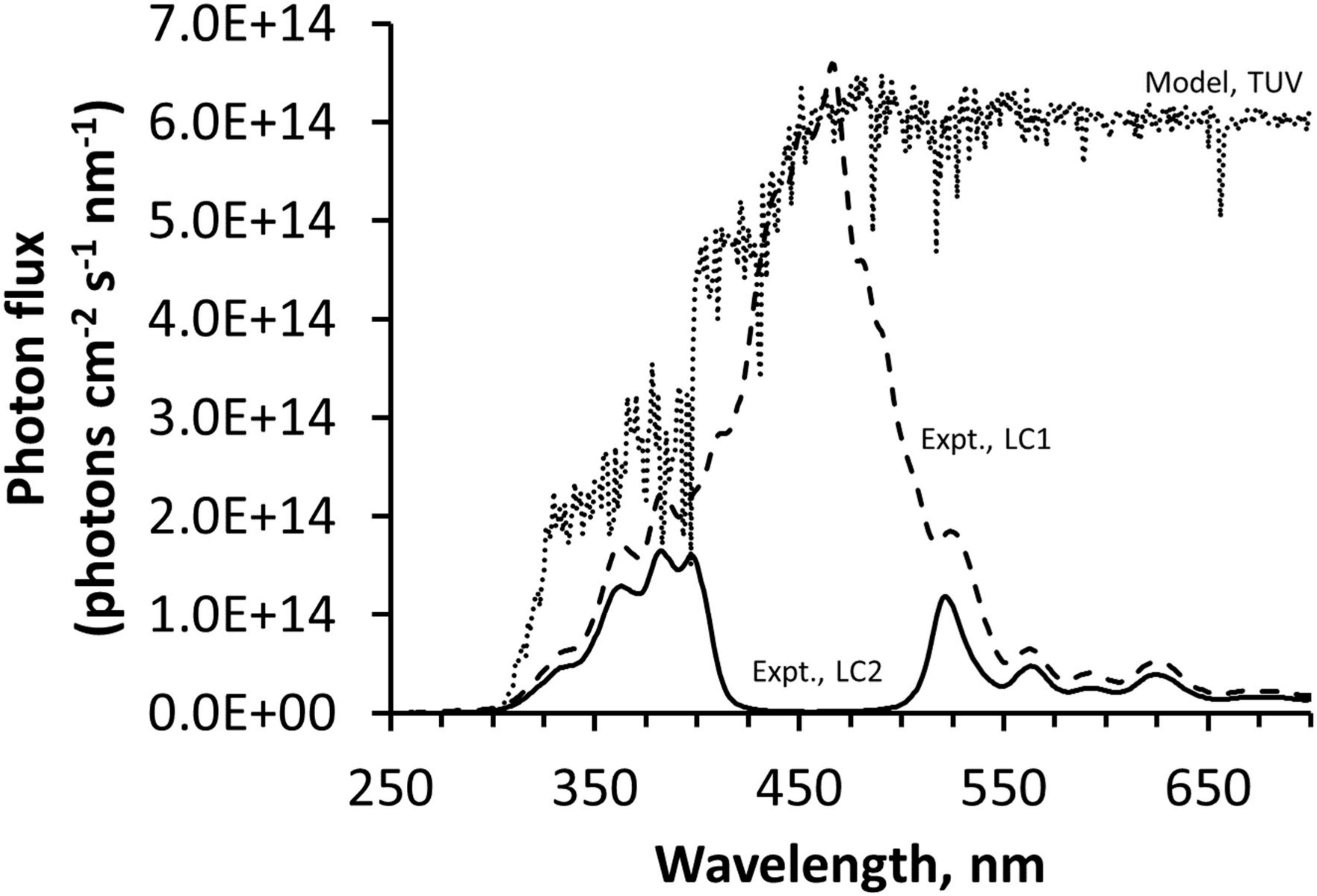

Supplementary Figure S5. Measured photon fluxes for our experimental setup (under light conditions LC1 and LC2) and the modeled actinic flux for Summit, Greenland, using the TUV model (Madronich and Flocke, 1998). Experimental photon flux has been normalized to a measured photon flux using the approach in Supplementary Section S1.

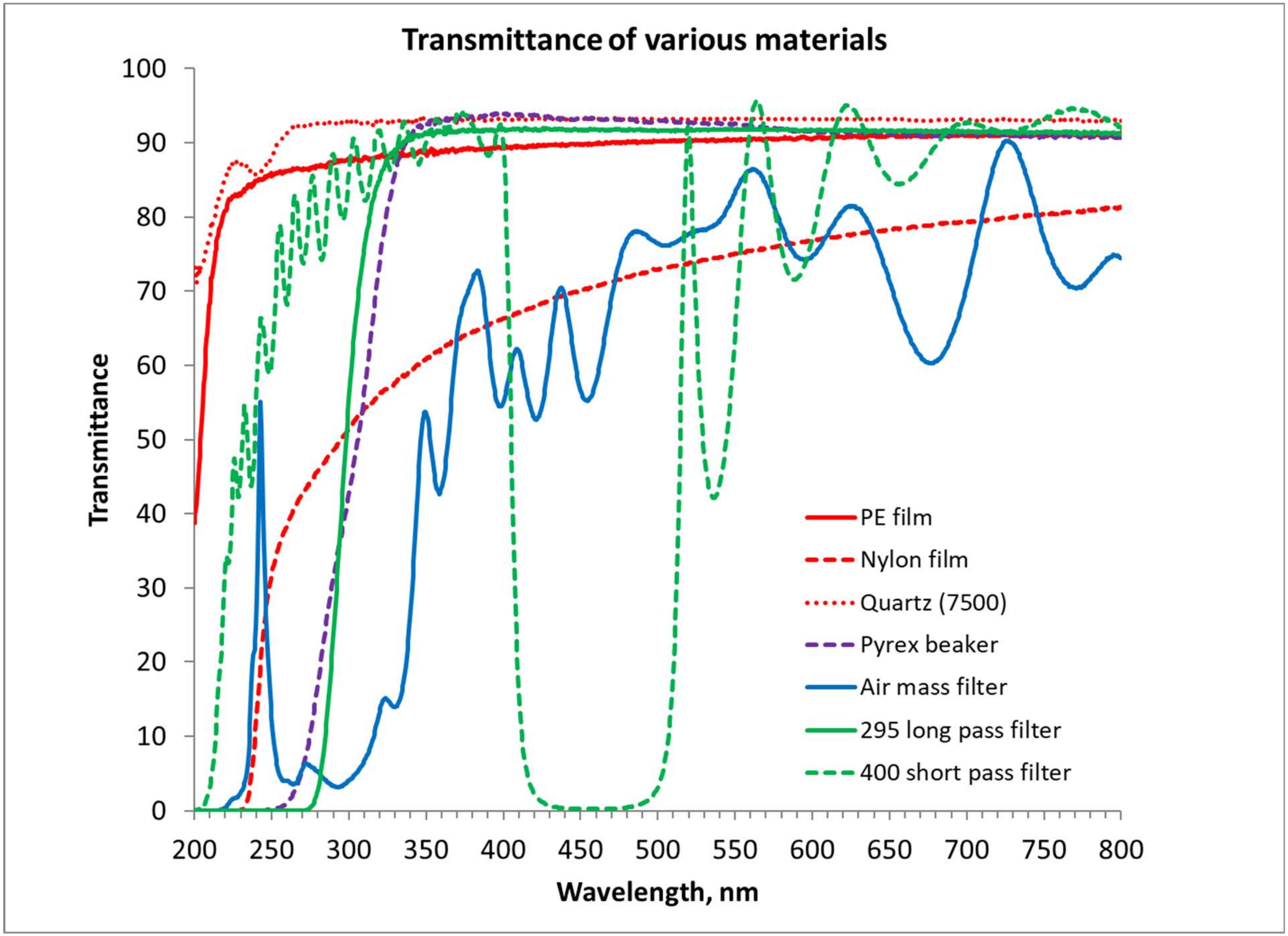

Supplementary Figure S6. Measured transmittance values for various materials, including the PE film used to cover the beakers, a thicker nylon film (not used in our experiments), a quartz plate, a Pyrex laboratory beaker, and several filters.

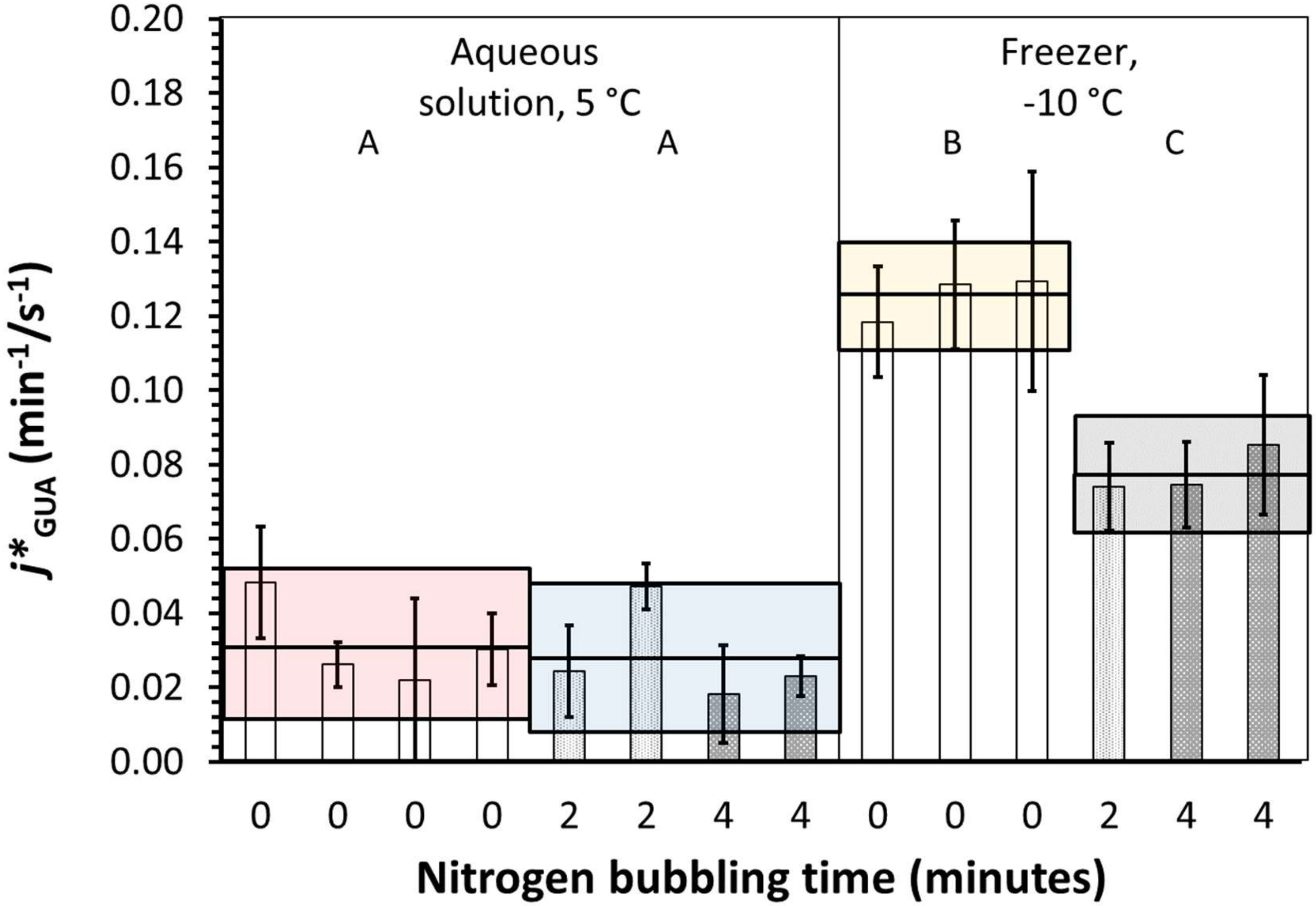

Supplementary Figure S7. *j**GUA determined for samples bubbled with nitrogen to reduce the concentration of dissolved oxygen. Samples were bubbled, capped, and then either illuminated as aqueous solution or frozen and then illuminated. Error bars are the propagated standard error (SE) of the experimental measurements. Colored regions indicate mean (central line) and 95% upper and lower confidence interval of the mean for each sample treatment group. Sample treatments with statistically indistinguishable average rate constants ($P < 0.05$) have the same capital letter, while treatments with different letters are statistically different.

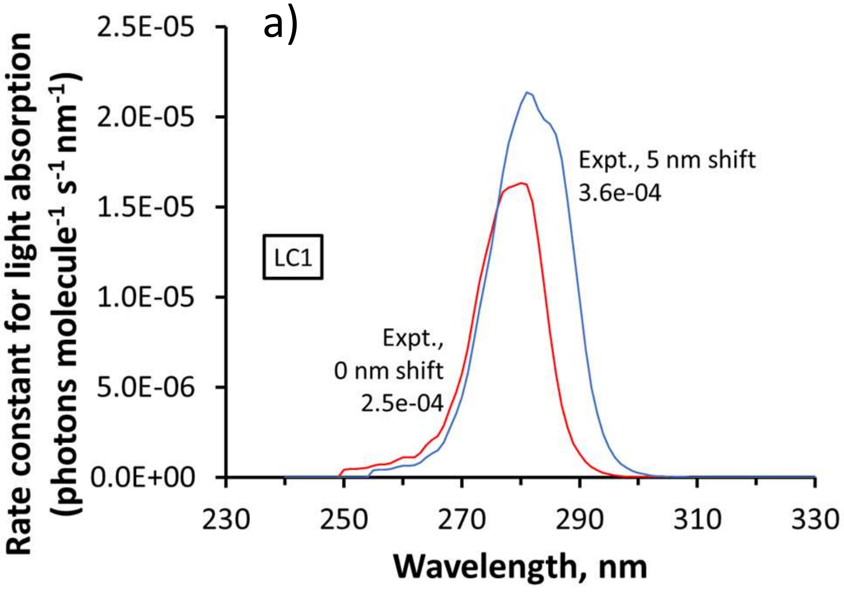

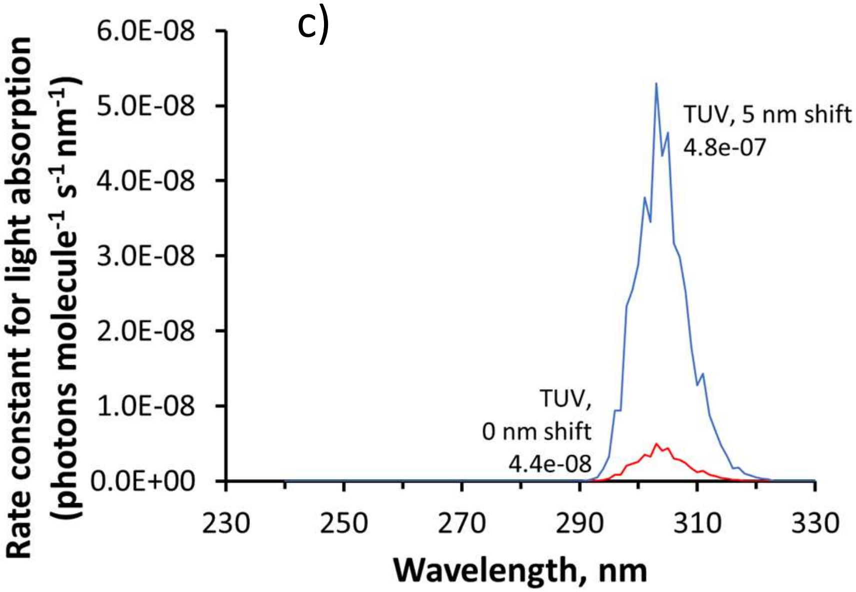

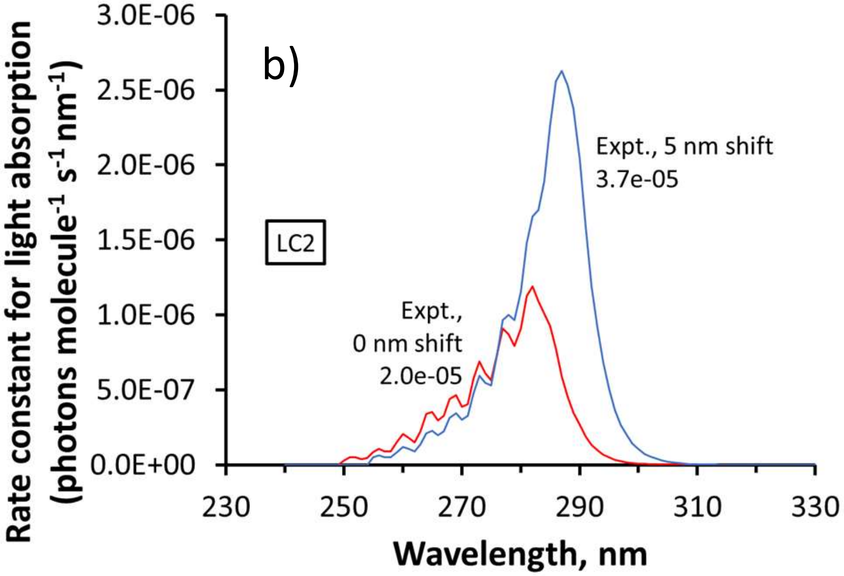

Supplementary Figure S8. Action spectra for light absorption, determined by multiplying the guaiacol molar absorptivity by the actinic flux at each wavelength. Red lines indicate the calculated action spectra for the guaiacol absorbance as measured; blue lines show the calculated action spectra assuming a 5 nm bathochromic (red) shift and a hyperchromic shift of ~6%. Numbers indicate the total amount of light absorbed (area under each curve, photons molecule^{-2} s^{-1}). a) Action spectra for LC1. b) Action spectra for LC2. c) Action spectra for the TUV modeled spectra.

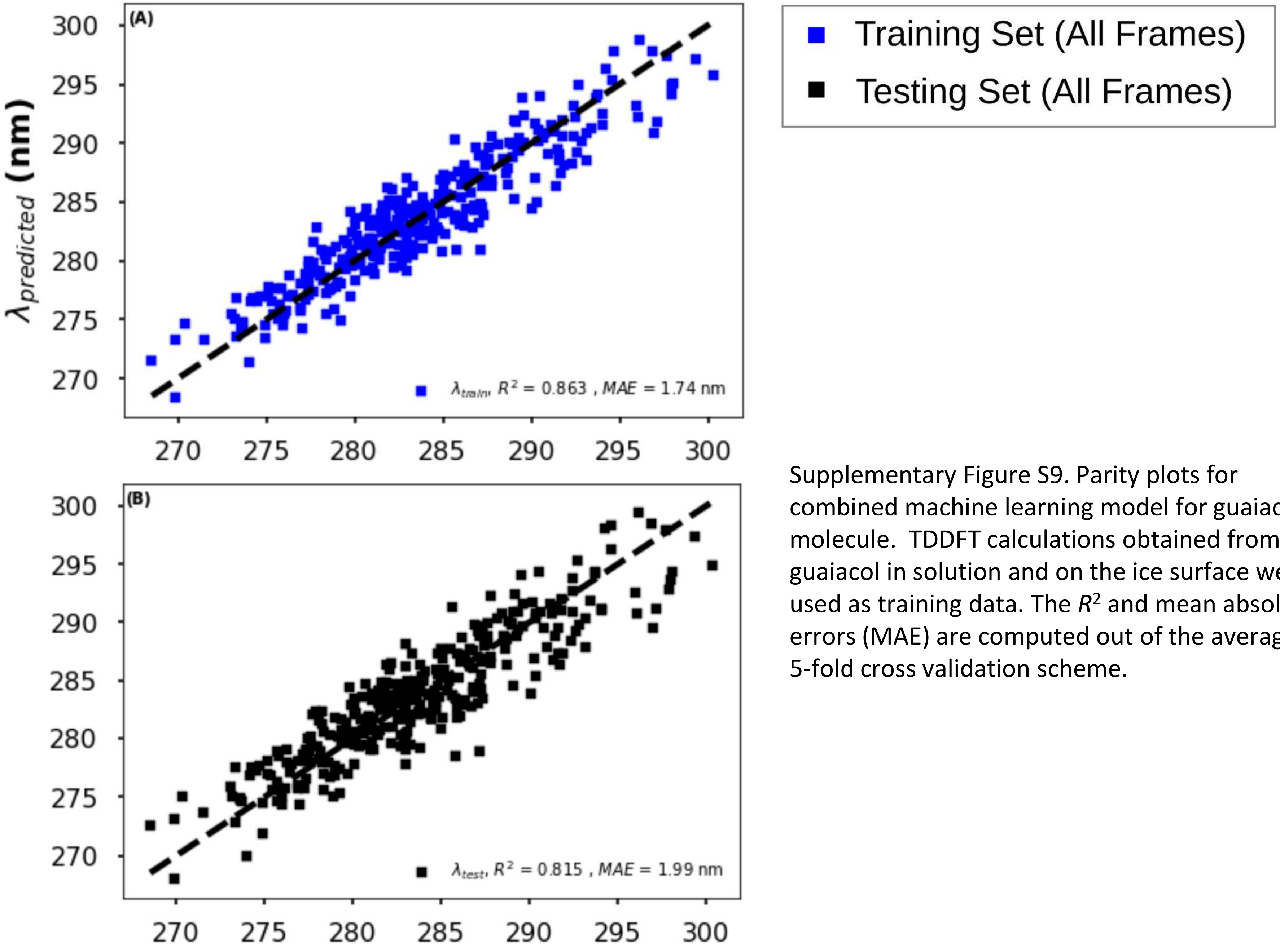

Supplementary Figure S9. Parity plots for combined machine learning model for guaiacol molecule. TDDFT calculations obtained from guaiacol in solution and on the ice surface were used as training data. The R^2 and mean absolute errors (MAE) are computed out of the average of 5-fold cross validation scheme.

References for Supplementary Information

1. Hutter, J., Iannuzzi, M., Schiffmann, F. & VandeVondele, J. CP2K: atomistic simulations of condensed matter systems. *Wiley Interdiscip. Rev. Comput. Mol. Sci.* **4,** 15–25 (2014).
2. Vandevondele, J. *et al.* Quickstep: Fast and accurate density functional calculations using a mixed Gaussian and plane waves approach. *Computer Physics Communications* **167,** 103–128 (Apr. 2005).
3. Plimpton, S. Fast Parallel Algorithms for Short-Range Molecular Dynamics. *J. Comp. Phys.* **117,** 1–19 (1995).
4. Bussi, G., Donadio, D. & Parrinello, M. Canonical sampling through velocity rescaling. *J. Chem. Phys.* **126,** 014101 (2007).
5. Perdew, J. P., Burke, K. & Ernzerhof, M. Generalized Gradient Approximation Made Simple. *Phys. Rev. Lett.* **77,** 3865–3868 (18 Oct. 1996).
6. Feller, D. The role of databases in support of computational chemistry calculations. *J. Comput. Chem.* **17.** doi:10.1002/(SICI)1096-987X(199610)17:13<1571::AID-JCC9>3.0.CO;2-P (1996).
7. Goedecker, S., Teter, M. & Hutter, J. Separable dual-space Gaussian pseudopotentials. *Phys. Rev. B* **54,** 1703–1710 (3 July 1996).
8. Timrov, I., Micciarelli, M., Rosa, M., Calzolari, A. & Baroni, S. Multimodel Approach to the Optical Properties of Molecular Dyes in Solution. *J. Chem. Theory Comput.* **12,** 4423–4429 (2016).
9. Ge, X. *et al.* Accurate and Inexpensive Prediction of the Color Optical Properties of Anthocyanins in Solution. *J. Phys. Chem. A* **119,** 3816–3822 (2015).
10. Malcıoğlu, O. B., Gebauer, R., Rocca, D. & Baroni, S. TurboTDDFT - A code for the simulation of molecular spectra using the Liouville-Lanczos approach to time-dependent density-functional perturbation theory. *Comput. Phys. Commun.* **182,** 1744–1754 (2011).
11. Giannozzi, P. *et al.* QUANTUM ESPRESSO: a modular and open-source software project for quantum simulations of materials. *J. Phys. Condens. Matter* **21,** 395502 (Sept. 2009).
12. Rocca, D., Gebauer, R., Saad, Y. & Baroni, S. Turbo charging time-dependent density-functional theory with Lanczos chains. *J. Chem. Phys.* **128,** 154105 (Apr. 2008).
13. Vanderbilt, D. Soft self-consistent pseudopotentials in a generalized eigenvalue formalism. **41,** 7892–7895 (Apr. 1990).
14. Martyna, G. J. & Tuckerman, M. E. A reciprocal space based method for treating long range interactions in ab initio and force-field-based calculations in clusters. *J. Chem. Phys.* **110,** 2810–2821 (Feb. 1999).
15. Andreussi, O., Dabo, I. & Marzari, N. Revised self-consistent continuum solvation in electronic-structure calculations. *J. Chem. Phys.* **136,** 064102 (2012).

References

16. Tibshirani, R. Regression shrinkage and selection via the lasso: a retrospective. *J. Royal Stat. Soc. B* **73,** 273–282 (June 2011).
17. E. S. Galbavy, K. Ram and C. Anastasio, 2-Nitrobenzaldehyde as a chemical actinometer for solution and ice photochemistry, *J. Photochem. Photobiol. A-Chem.*, 2010, **209**, 186-192.
18. T. Hullar, D. Magadia and C. Anastasio, Photodegradation Rate Constants for Anthracene and Pyrene Are Similar in/on Ice and in Aqueous Solution, *Environ. Sci. Technol.*, 2018, **52**, 12225-12234.
19. H. Nakamura, A new apparatus to produce fresh snow, *Rep. Natl Res. Cent. Disaster Prev.*, 1978, **19**, 229-237.
20. S. Schleef, M. Jaggi, H. Lowe and M. Schneebeli, An improved machine to produce nature-identical snow in the laboratory, *J. Glaciol.*, 2014, **60**, 94-102.